Relativistic eigenchannel *R*-matrix studies of the strong intrashell electron correlations in highly charged Ar^{13+} ions

Li-Jun Dou,[1,2] Rui Jin,[3,4,*] Rui Sun,[4] Lu-You Xie,[5] Zhong-Kui Huang,[1] Jia-Ming Li,[4,6,7] Xin-Wen Ma,[1,8,†] and Xiang Gao[2,9,‡]

[1]*Institute of Modern Physics, Chinese Academy of Sciences, Lanzhou, 730000, China*
[2]*Beijing Computational Science Research Center, Beijing 100193, China*
[3]*Center for Free-Electron Laser Science, DESY, Notkestrasse 85, D-22607 Hamburg, Germany*
[4]*Key Laboratory for Laser Plasmas (Ministry of Education) and Department of Physics and Astronomy, Shanghai Jiao Tong University, Shanghai 200240, China*
[5]*College of Physics and Electronic Engineering, Northwest Normal University, Lanzhou, 730070, China*
[6]*Department of Physics and Center for Atomic and Molecular Nanosciences, Tsinghua University, Beijing 100084, China*
[7]*Collaborative Innovation Center of Quantum Matter, Beijing 100084, China*
[8]*University of Chinese Academy of Sciences, Beijing, 100049, China*
[9]*Institute for Theoretical Physics, Vienna University of Technology, A-1040 Vienna, Austria, European Union*

(Received 21 June 2019; revised manuscript received 20 February 2020; accepted 20 February 2020; published 17 March 2020)

Highly charged ion systems play an important role in simulation and diagnostics of astrophysical and fusion plasmas. Due to dominant strong Coulomb interactions from the nuclear charge, electron correlations are generally thought to be less prominent than relativistic effects and other effects in HCIs. In this paper, we demonstrate the importance of strong intrashell electron correlations from the quasidegeneracy of $2s$, $2p$ orbitals in highly charged B-like Ar^{13+} ions. Such strong intrashell electron interactions manifest as an atomic system with many channel interactions, which will ultimately form a much more complex atomic spectrum than the neutral B atom in the isoelectronic sequence. As a typical example, the relativistic eigenchannel *R*-matrix method (R-R-eigen code) was successfully applied to investigate the complex spectrum of Ar^{13+} ions with $J^\pi = 1.5^+$ symmetry in discrete and autoionization regions. Calculated results obviously show interesting behaviors of strong intrashell electron correlations in HCIs. Additionally, it is also beneficial to understand discrepancies in the low-energy electron-ion recombination spectra of Be-like Ar^{14+} ions between experimental observations at the main cooler-storage ring of the Heavy Ion Research Facility in Lanzhou and distorted wave calculation.

DOI: 10.1103/PhysRevA.101.032508

I. INTRODUCTION

Highly charged ions (HCIs) play an important role in astrophysics and fusion plasmas. Related atomic data on energy levels, autoionization widths, oscillator strengths, and collision rates (electron impact excitation, electron-ion recombination, etc.) are required to numerically simulate temporal-spatial motions for plasmas in astrophysical objects or controlled fusion facilities. They are also needed for diagnostic analysis of plasma parameters [1–6]. For example, argon ($Z = 18$) is one of the most abundant heavy elements in the universe. Emission lines from argon have been observed and were applied for plasma diagnostics [6,7].

Comparing with relativistic effects (scale as Z^2 and higher), the electron correlation effects (scaling as Z) are generally less prominent in HCIs than that in lowly charged ions along the isoelectronic sequence. However, considering the strong Coulombic field within HCIs, their orbitals are generally similar to orbitals of hydrogenlike ions with the same ionization degree, i.e., orbital energies for orbitals with the same principal quantum number n are almost degenerate. Thus, it is reasonable to believe that intrashell electron correlations would play an important role in HCI energy-level structures, which may show more complicated structures and different features compared to lowly charged ions. As an illustrative example, we show in Fig. 1 the excited energy structure of the B-like neutral B atom and Ar^{13+} ion to display different electron correlation features in lowly and highly charged ions, respectively. For the open-shell B atom with one active electron in a specific J^π (left), bound-state levels below the first ionization threshold $(2s^2)^1S^e$ (at zero of the scaled energy) all belong to the single channel $(2s^2)\ ^1S^e\,nl$. In contrast, for Ar^{13+} ions (right), all channel states squeeze together, which indicates a strong mixing among these channels, including $(2s^2)\ ^1S^e\,nl$, $(2s2p)\ ^3P^o\,nl$, $^1P^o\,nl$, $(2p^2)\ ^3P^e\,nl$, $^1D^e\,nl$, $^1S^e\,nl$. Similar differences also exist in autoionization resonant states above the first ionization threshold. Such features of HCI energy levels raise another challenge for theoretical treatments in addition to electron correlations. Specifically, the density of

*rui.jin@cfel.de
†x.ma@impcas.ac.cn
‡xgao@csrc.ac.cn

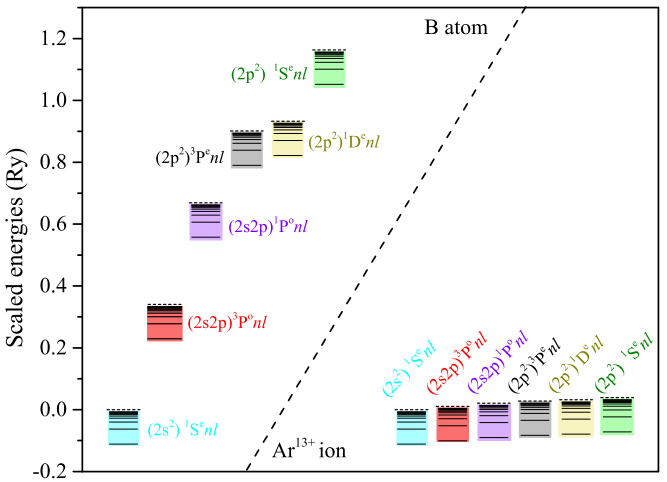

FIG. 1. Schematic diagram of $2l2l'nl''$ Rydberg states in the $1/(q+1)^2$ scaled energy of neutral B atom (left) and B-like Ar^{13+} ion (right), with q the ionization degree. The first threshold $(2s^2)\ ^1S^e$ is chosen as the zero energy for the scaled energy. Both systems show the similar Rydberg series $(2s^2)\ ^1S^e nl$, $(2s2p)\ ^3P^o nl$, $^1P^o nl$ and $(2p^2)\ ^3P^e nl$, $^1D^e nl$, $^1S^e nl$, represented by solid lines converging to the associated six thresholds (dashed lines). The Ar^{13+} system obviously shows quasidegeneracy of the thresholds, giving rise to complex electron-electron interactions.

states of HCIs in energy regions containing these intrashell states is much larger than that of lowly charged ions. Then with the same experimental energy resolution, many more bound or resonant states are required to be considered for relevant physical processes. Based on the discussion above, one is not surprised by recent precision electron-ion recombination experiments of Be-like Ar^{14+} ions at the main cooler-storage ring (CSRm), where substantial discrepancies existed between measured recombination rates and theoretical results calculated by the distorted wave (DW) method [7]. Thus, a theoretical method which can treat these intrashell electron correlations adequately and provide accurate resonance positions as well as autoionization rates efficiently is urgently required for a better understanding of measured recombination spectra of HCIs.

Based on analytical continuation properties of short-range scattering matrices, we have developed the relativistic eigenchannel R-matrix method (R-R-eigen code) [8–14], which has been successfully applied for many atomic processes, such as electron impact excitations [8,9], photoionizations [10,11,14], etc. In this method, we first calculate short-range scattering matrices, i.e., physical parameters associated with the multichannel quantum defect theory (MQDT) [15–21], and related wave functions for both discrete and continuous energy regions of interest. Then, various physical quantities can be derived from a straightforward application of the MQDT procedure [15–21]. Since short-range scattering matrices in the discrete energy region can be examined stringently by precise spectroscopic data using analytical properties of short-range scattering matrices, scattering matrices in the continuum energy region can be readily obtained with desired accuracies. Note that short-range scattering matrices vary smoothly with energy because of their analytical continuation properties. Therefore, the excited bound states and adjacent continua can be treated in a unified way. One only needs to calculate short-range scattering matrices in a few energy grid samples over the energy regions of interest, which is one unique merit of this method. Therefore, the R-R-eigen method is very promising for calculating dense resonant states of HCIs.

In this work, we use the R-R-eigen method to investigate bound energy levels as well as autoionization resonances of highly charged Ar^{13+} ions with $J^\pi = 1.5^+$ symmetry. Strong electron correlations within $2s$, $2p$ shells are demonstrated through calculated complex multichannel energy structures.

II. THEORETICAL METHODS AND CALCULATION RESULTS

A. Calculation of eigenchannel parameters

The relativistic eigenchannel R-matrix method (R-R-eigen) [8–14] is applied in this study to stringently treat the complex atomic multielectron problem. Briefly, the coupling of N-electron ion-core target states and an excited electron with the appropriate angular momentum forms channels for the $N+1$-electron excited complex with a specific total angular momentum. The multichannel logarithmic derivative boundary matrix $R(E)$ is obtained by solving the $N+1$-electron problem variationally within the R-matrix box, i.e., the reaction zone. With the $R(E)$ matrix, the reaction matrix $K(E)$ can be calculated with the appropriate standing-wave expressions on the boundary of the reaction zone.

Our R-R-eigen method [8–14] differs from the traditional R-matrix method [22–27] mainly by definitions of physical channels, which includes not only opened channels (with positive orbital energies) but also several relevant closed channels (with negative orbital energies). Therefore, physical channels (the number of which is denoted as n_p) include all Rydberg-type bound electrons and their adjacent continua with orbital energy in the energy range of $\varepsilon > -q^2/l^2$ (in Ry, where q is the charge of a long-range potential and l is the orbital angular momentum of the electron) owing to the mathematical properties of Coulomb wave functions [20]. Other closed channels with deep negative orbital energies and $N+1$ bound-type configurations are also included as computational channels (the number of which is denoted as $n_{\rm com}$) to consider electron correlations adequately. Once the number of target states is determined, the total number of channels $n_{tot} = n_p + n_{\rm com}$ is determined and remains unchanged throughout calculations. The number of physical channels n_p will increase with the energy to meet the energy criteria $\varepsilon > -q^2/l^2$. The $n_p \times n_p$ scattering matrices can be readily calculated with a suitably chosen physical channel set for certain energies, which have the analytical continuation properties. The short-range scattering matrix K^{J^π} for the symmetry block with the total angular momentum J and parity π can be expressed in the diagonal representation by

$$K_{ij}^{J^\pi} = \sum_\alpha U_{i\alpha} \tan(\pi\mu_\alpha) U_{j\alpha}, \tag{1}$$

with the n_p eigenquantum defect μ_α and transformation matrix $U_{i\alpha}$ represented by Euler-type angles θ_k, $k = 1, \ldots, n_p(n_p-1)/2$ [16]. The μ_α and $U_{i\alpha}$ are so-called physical parameters in the MQDT procedure [15–21].

TABLE I. Physical channels (ionization channel) and corresponding eigenchannels for Ar^{13+} ions with $J^\pi = 1.5^+$.

Index	1	2	3	4	5	6	7	8	9
Ionization channels	$^1S^e_0\, d_{3/2}$	$^3P^o_0\, p_{3/2}$	$^3P^o_1\, p_{1/2}$	$^3P^o_1\, p_{3/2}$	$^3P^o_2\, p_{1/2}$	$^3P^o_2\, p_{3/2}$	$^1P^o_1\, p_{1/2}$	$^1P^o_1\, p_{3/2}$	$^3P^e_1\, s$
Eigenchannels	$^1S^e\, d\ \ ^2D$	$^3P^o\, p\ \ ^4S$	$^3P^o\, p\ \ ^4D$	$^3P^o\, p\ \ ^2D$	$^3P^o\, p\ \ ^4P$	$^3P^o\, p\ \ ^2P$	$^1P^o\, p\ \ ^2D$	$^1P^o\, p\ \ ^2P$	$^3P^e\, s\ \ ^4P$
Index	10	11	12	13	14	15	16	17	18
Ionization channels	$^3P^e_2\, s$	$^1D^e_2\, s$	$^3P^e_0\, d_{3/2}$	$^3P^e_1\, d_{3/2}$	$^3P^e_1\, d_{5/2}$	$^3P^e_2\, d_{3/2}$	$^3P^e_2\, d_{5/2}$	$^1D^e_2\, d_{3/2}$	$^1D^e_2\, d_{5/2}$
Eigenchannels	$^3P^e\, s\ \ ^2P$	$^1D^e\, s\ \ ^2D$	$^3P^e\, d\ \ ^4F$	$^3P^e\, d\ \ ^4D$	$^3P^e\, d\ \ ^2D$	$^3P^e\, d\ \ ^4P$	$^3P^e\, d\ \ ^2P$	$^1D^e\, d\ \ ^2D$	$^1D^e\, d\ \ ^2P$
Index	19	20	21	22	23	24	25		
Ionization channels	$^1S^e_0\, d_{3/2}$	$^3P^o_1\, f_{5/2}$	$^3P^o_2\, f_{5/2}$	$^3P^o_2\, f_{7/2}$	$^1P^o_1\, f_{5/2}$	$^3P^e_2\, g_{7/2}$	$^1D^e_2\, g_{7/2}$		
Eigenchannels	$^1S^e\, d\ \ ^2D$	$^3P^o\, f\ \ ^4F$	$^3P^o\, f\ \ ^4D$	$^3P^o\, f\ \ ^2D$	$^1P^o\, f\ \ ^2D$	$^3P^e\, g\ \ ^4F$	$^1D^e\, g\ \ ^2D$		

For our interested energy regions, we consider all possible electron configurations with $2s$, $2p$ shells of Ar^{14+} targets for intrashell correlations, i.e., Ar^{14+} $(2s^2)\ ^1S^e_0$, $(2s2p)\ ^3P^o_{0,1,2}$, $(2s2p)\ ^1P^o_1$, $(2p^2)\ ^3P^e_{0,1,2}$, $(2p^2)\ ^1D^e_2$, $(2p^2)\ ^1S^e_0$ with energies 0.00, 2.0839, 2.1493, 2.3026, 4.1206, 5.5124, 5.6056, 5.7256, 6.2843, 7.6603 Ry [28,29], respectively. As the scattering energy varies from the bound-state region below the first ionization threshold $(2s^2)\ ^1S^e_0$ to the complete continuum-state region above the highest threshold $(2p^2)\ ^1S^e_0$ via the intermediate autoionization region, the number of physical channels n_p varies from 1, 6, 8, 11, 19, 22, 23, to 25, which forms eight energy regions for the short-range scattering matrix calculations. To facilitate later discussions with variable physical channels, all 25 ionization channels (JJ notation) are listed in Table I with their corresponding eigenchannels (LS notation), respectively. Here orders of ionization channels are arranged to comply with physical channels used in calculations with the increasing energy, and related eigenchannel labels are given by their maximum overlap component with the geometric JJ decomposition representing corresponding ionization channels. Calculated eigenquantum defects μ in the energy range from -23.0 to 8.0 Ry are displayed in Fig. 2. Considering the number of channels involved in our calculation is relatively large, we show the figure of corresponding Euler-type angles θ_k (as well as the data of scattering matrices) in the Supplemental Material [30].

As can be seen, MQDT parameters (μ_α and θ_k) vary smoothly within each energy region and cross ten ionization thresholds smoothly, which well reflect the analytical properties of the calculated scattering matrices. Additionally, parameters of two adjacent energy regions connect perfectly with each other over intersection regions for $1 \leftrightarrow 6$, $11 \leftrightarrow 19$, $19 \leftrightarrow 22$, $22 \leftrightarrow 23$, and $23 \leftrightarrow 25$ channels, which are denoted as the type-I connection with weak interchannel interactions [12]. However, for $6 \leftrightarrow 8$ and $8 \leftrightarrow 11$ channels, newly added-on physical channels strongly interacted with

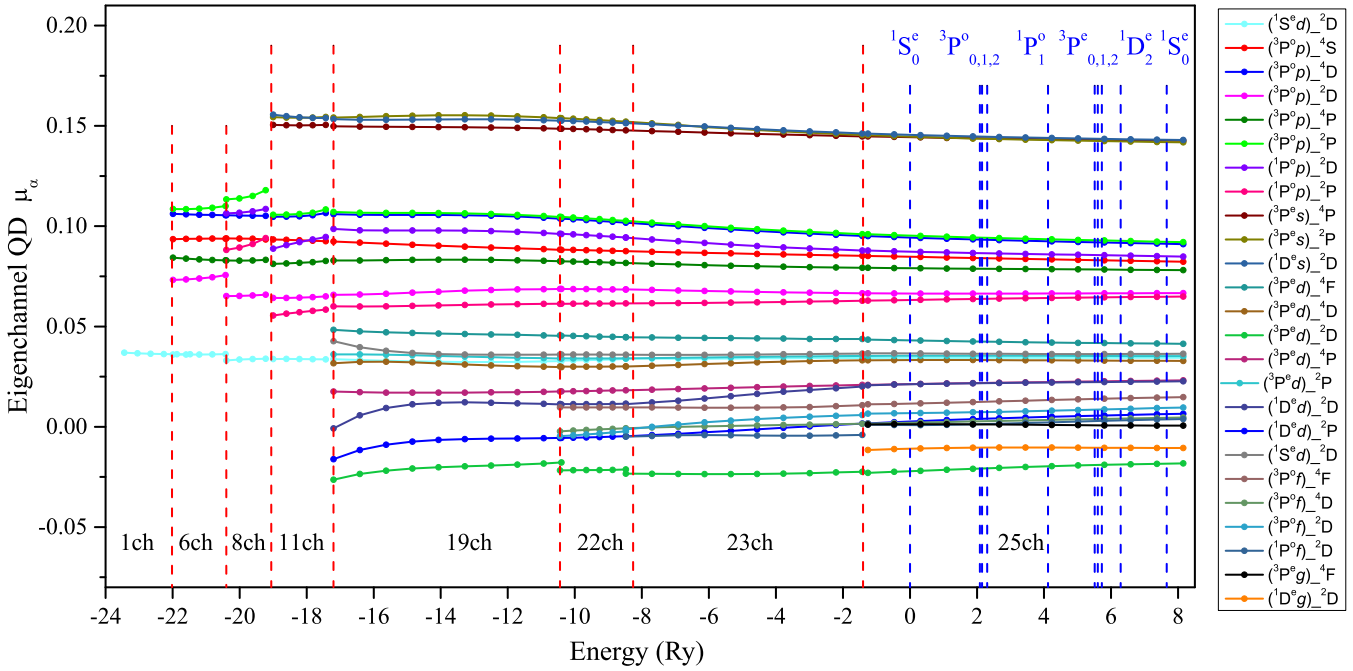

FIG. 2. MQDT physical parameters (eigenquantum defects μ_α of scattering matrices) of Ar^{13+} system with $J^\pi = 1.5^+$ in both discrete and autoionization energy regions ($-23.0 \leqslant E \leqslant 8.0$ Ry) across ten thresholds represented by the vertical dashed blue lines. The vertical dashed red lines plotted at $E = -22.0, -20.4, -19.1, -17.2, -10.4, -8.3$, and -1.8 Ry give boundaries of individual eight energy regions. See the main text for more details.

previous ones, inducing the so-called type-II connection [12]. Compared to eigenquantum defects μ_α, Euler-type angles θ_k (see Supplemental Material [30]) are more sensitive to the energy due to relatively strong interchannel interactions at 8ch, 11ch, and 19ch regions. Based on analytical continuation properties of scattering matrices, all discrete energy levels and autoionization resonances can be obtained without missing any one in the framework of the MQDT. On the other hand, one can readily check/calibrate the accuracy of scattering matrices using available spectroscopic data [9,13,14].

B. Calculation of discrete energy levels and the assessment of accuracies of eigenchannel parameters with spectroscopy data

The eigenchannel wave functions $\Psi_\alpha^{J^\pi}$ inside the reaction zone ($r \leqslant r_0$) are calculated variationally [8–14]. Outside the reaction zone ($r \geqslant r_0$), it can be expressed rigorously as

$$\Psi_\alpha^{J^\pi} = \sum_{i=1}^{n_p} \Phi_i \cdot U_{i\alpha} \cdot (f_i \cos\pi\mu_\alpha - g_i \sin\pi\mu_\alpha), \qquad (2)$$

where f_i and g_i are regular and irregular Coulomb functions, respectively, and Φ_i represents the channel wave function. Wave functions of physical states (energy eigenstates) can be expressed as the linear combination of eigenchannel wave functions $\Psi_\alpha^{J\pi}$ [8–14,20,21],

$$\Psi^{J^\pi}(E) = \Sigma_\alpha A_\alpha \Psi_\alpha^{J\pi}(E), \qquad (3)$$

where mixing coefficients A_α can be determined from asymptotic boundary conditions [15–21]. For bound states, all channels are closed, and the asymptotic boundary conditions require

$$\Sigma_\alpha U_{i\alpha} \sin\pi(\nu_i + \mu_\alpha) A_\alpha = 0, \quad \text{for all } i, \qquad (4)$$

with the effective principal quantum numbers ν_i defined as

$$E = I_i - q^2/\nu_i^2 \quad (\text{in Ry}), \qquad (5)$$

where I_i is the threshold and q is the charge of the target ions. The existence of nontrivial A_α leads to the MQDT equation:

$$F(\{\nu_i\}, \{U_{i\alpha}, \mu_\alpha\}) = \det[U_{i\alpha} \sin\pi(\nu_i + \mu_\alpha)] = \det(F_{i\alpha}) = 0. \qquad (6)$$

In principle, although one can obtain theoretical energy levels by solving Eqs. (5) and (6) with the substitution-elimination method, it is not convenient for a systematic overview of level characteristics and checking the calculation accuracy with the precision spectroscopy data. Instead, we can use our proposed "projected high dimensional quantum-defect graph (symmetrized)" (JHANGZ plot) method as a multithreshold generalization of the Lu-Fano plot to solve Eqs. (5) and (6) [14]. This semianalytical method facilitates a visual comparison of theoretical results with experiment data systematically, where the effective quantum defect is applied to represent energy positions. It allows one to readily check and/or calibrate an *ab initio* calculated scattering matrix. In addition, the complex overlapping resonances can be systematically analyzed using the JHANGZ plot. A detailed discussion on the JHANGZ plot can be found in Ref. [14]. In short, we can use energy constraints from Eq. (5) to project the multiple unknown variables in Eq. (6) onto a two-dimension subspace. There is a parameter I_{one} representing one of the ionization thresholds to control the general geometric structure of this plot. Channels associated with thresholds higher than I_{one} will behave as resonances, while the others are nonresonant curves. Then, the projected two-dimension subspace can be spanned by any two effective principle quantum numbers in principle. However, a better choice of abscissa and ordinate (determined by I_{one}) can greatly simplify the physical analysis and illustrate the merits of eigenchannel treatments. Taking $J^\pi = 1.5^+$ as an example, instead of choosing the effective principle quantum number associated with the first threshold $^1S_0^e$ as I_{one}, we choose the third one, $^3P_1^o$, to show moderately dense resonances. Effective principle quantum numbers associated with the first and second thresholds are projected out in Eq. (6) with the following two energy constraints:

$$\begin{aligned}\Delta_1 \equiv \nu_{^1S_0^e} - \nu_{^3P_1^o} &= \left[1/\nu^2_{^3P_2^o} - \left(I_{^3P_2^o} - I_{^1S_0^e}\right)/q^2\right]^{-\frac{1}{2}} \\ &\quad - \left[1/\nu^2_{^3P_2^o} - \left(I_{^3P_2^o} - I_{^3P_1^o}\right)/q^2\right]^{-\frac{1}{2}}, \\ \Delta_2 \equiv \nu_{^3P_0^o} - \nu_{^3P_1^o} &= \left[1/\nu^2_{^3P_2^o} - \left(I_{^3P_2^o} - I_{^3P_0^o}\right)/q^2\right]^{-\frac{1}{2}} \\ &\quad - \left[1/\nu^2_{^3P_2^o} - \left(I_{^3P_2^o} - I_{^3P_1^o}\right)/q^2\right]^{-\frac{1}{2}}. \end{aligned} \qquad (7)$$

The main abscissa is chosen as $\nu_{^3P_0^o}$, and the other effective principal quantum numbers can be used as auxiliary abscissa.

Figure 3 shows the JHANGZ plot ($\nu_{^3P_0^o}$, $\nu_{^3P_1^o}$) for an Ar^{13+} system with $J^\pi = 1.5^+$ to check and/or calibrate scattering matrices in the discrete energy region. Quasiperiodic resonant colored branch curves are solutions of determinant Eq. (6) under additional constraining conditions of Eq. (7). And the gray dashed lines show the energy relation between $\nu_{^3P_1^o}$ and $\nu_{^3P_0^o}$ according to Eq. (5), i.e., $I_{^3P_1^o} - 14^2/\nu^2_{^3P_1^o} = I_{^3P_0^o} - 14^2/\nu^2_{^3P_0^o}$ in the discrete region. The crossing points of these two set of lines are our calculated energy-level positions. As can be seen, the energy-level structures are very complicated due to strong intrashell electron correlations. With the aid of our calculated A_α coefficients, we can get the detailed information regarding the complex channel interactions. For example, the physical channel characteristics of these solution curves (represented by different colors and symbols) are determined by ionized-channel coefficients with $A_i = \sum_\alpha U_{i\alpha} A_\alpha$. Specifically, different color curves, including cyan, red, green, violet, black, magenta, orange, dark yellow, and olive, represent channels with thresholds $(2s^2)\ ^1S_0^e$, $(2s2p)\ ^3P_{0,1,2}^o$, $(2s2p)\ ^1P_1^o$, $(2p^2)\ ^3P_{0,1,2}^e$, $(2p^2)\ ^1D_2^e$, and $(2p^2)\ ^1S_0^e$, respectively. And different symbols, namely, circle, left-triangle, right-triangle, down-triangle, up-triangle, square, diamond, and pentagon, indicate physical states with channel electrons s, $p_{1/2}$, $p_{3/2}$, $d_{3/2}$, $d_{5/2}$, $f_{5/2}$, $f_{7/2}$, and $g_{7/2}$, respectively. Eight auxiliary abscissas ($\nu_{^3P_1^o}$, $\nu_{^3P_2^o}$, $\nu_{^1P_1^o}$, $\nu_{^3P_0^e}$, $\nu_{^3P_1^e}$, $\nu_{^3P_2^e}$, $\nu_{^1D_2^e}$, and $\nu_{^1S_0^e}$) also help to determine states by showing the principal quantum number of related channel electrons. All of the above can make the identification of bound states quick and clear in the JHANGZ plot. It can be seen that there are four solutions for 6-, 8-, 11-, and 19-channel energy regions and five for higher energy regions (cyan, red, and blue lines associated with three thresholds $^1S_0^e$, $^3P_{0,1}^o$). Because of the energy

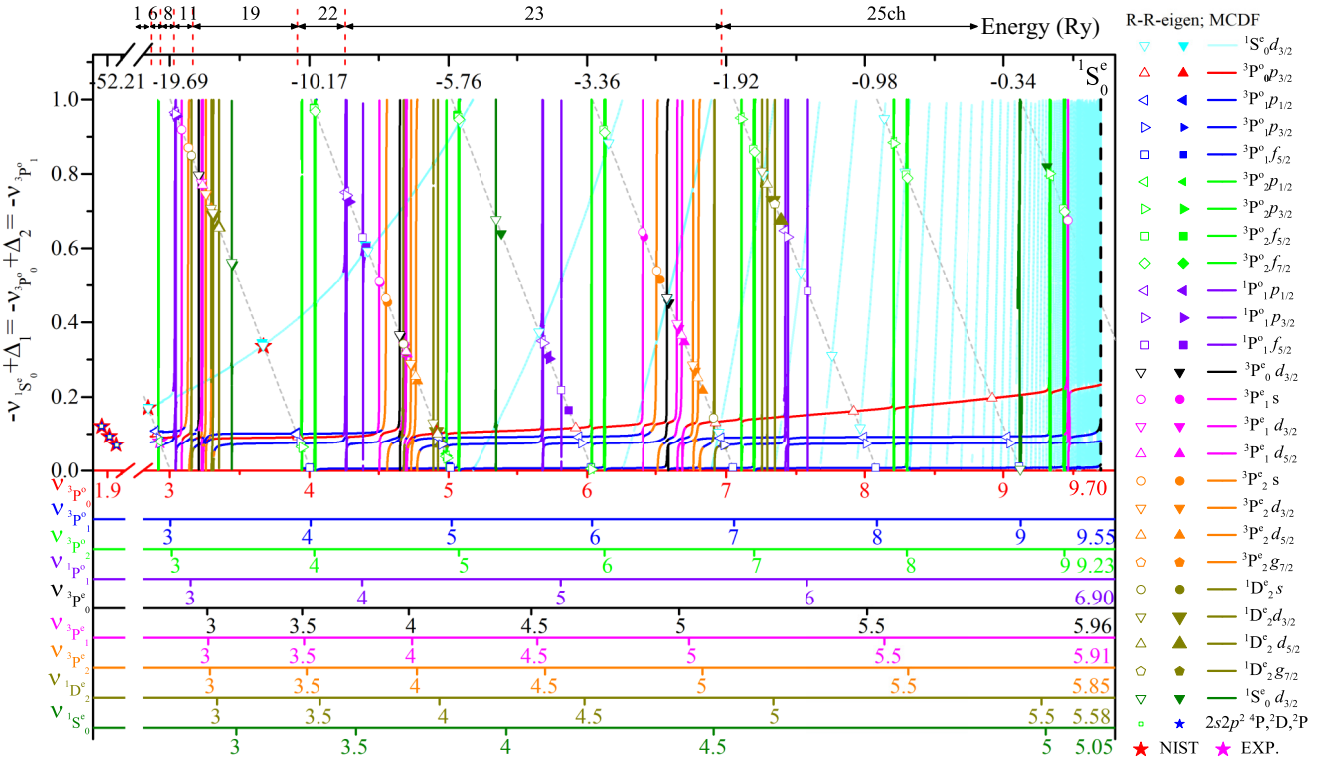

FIG. 3. Projected high-dimensional quantum-defect graph (symmetrized) (i.e., JHANGZ plot) for Ar^{13+} ions with $J^\pi = 1.5^+$ for the demonstration of discrete energy-level calculations and the assessment of the scattering matrix accuracy. Quasiperiodic resonant colored branch curves are solutions of the determinant Eq. (6) under the energy constraint of Eq. (7), where different colors and symbols indicate related thresholds and channel electrons involved, respectively. The gray dashed lines represent the energy relation between $\nu_{^3P_1^o}$ and $\nu_{^3P_0^o}$ from Eq. (5) by $I_{^3P_1^o} - 14^2/\nu^2_{^3P_1^o} = I_{^3P_0^o} - 14^2/\nu^2_{^3P_0^o}$. All theoretical energies are obtained at intersections between solution curves and energy relation lines (using *ab initio* calculated MQDT parameters in Fig. 2 without the calibration), which are indicated as opened symbols. For comparison, available experimental energy levels [29,31] and MCDF results [32] are indicated as solid symbols. Here auxiliary abscissas associated with all thresholds ($\nu_{^3P_0^o}$, $\nu_{^3P_1^o}$, $\nu_{^3P_2^o}$, $\nu_{^1P_1^o}$, $\nu_{^3P_0^e}$, $\nu_{^3P_1^e}$, $\nu_{^3P_2^e}$, $\nu_{^1D_2^e}$ and $\nu_{^1S_0^e}$) are plotted for the convenience of characterizing states.

constraint in Eq. (7), the cyan branch curve goes up-tilted quickly with the increasing energy and converges to its threshold $^1S_0^e$. Red branch curves associated with the second threshold $^3P_0^o$ go up-tilted much more slowly. In contrast, blue curves associated with the third threshold $^3P_1^o$ appear as a nearly "horizontal" lines, which will converge to their thresholds in higher energy regions. Other channels with higher thresholds $^3P_2^o$, $^1P_1^o$, $^3P^e_{0,1,2}$, $^1D_2^e$, $^1S_0^e$ form locally isolated resonances at the position where the effective principal quantum number $\nu \approx$ integer (green, violet, black, magenta, orange, dark yellow, and olive curves, respectively).

The opened color symbols at intersection points of solid solution curves [Eqs. (6) and (7)] and gray dashed lines [Eq. (5)] represent all our calculated energy levels of highly charged Ar^{14+} ions. As a comparison, related experimental data from NIST [29] (red stars) and Ref. [31] (magenta stars) and multiconfiguration Dirac-Fock (MCDF) results [32] (solid symbols) are all displayed here. Besides, three isolated leading states $(2s2p)\ ^4P$, ^2D, ^2P are in the energy region even lower than the present one-channel region $\nu_{^3P_0^o} \approx 1.80$. In practice, simply extrapolating the scattering matrix and adapting the MQDT graphical procedure would not give a satisfactory result. Thus, we directly apply the traditional *R*-matrix method [22–27] to calculate bound states, indicated as green opened squares in Fig. 3. Comparing the *R*-matrix results with NIST data [29], great agreement can be found within 0.1%. Additionally, MCDF results are also in good agreement with the spectroscopy data [29,31] in higher energy regions. However, we already notice that the agreement between MCDF results and the experimental data [29] for the highest $(2s^24d)\ ^2D$ state at $\nu_{^3P_0^o} \approx 3.67$ is worse than our R-R-eigen result. Because of analytical continuation properties of scattering matrices, we can anticipate that all energy levels should be calculated with the similar accuracy as the lower six levels. On the other hand, MCDF results do not have this unique property. For example, our R-R-eigen calculation of $^1S_0^e\ 5d_{3/2}$ (olive down-triangle) at $\nu_{^3P_0^o} = 9.1208\ (-3.7032\ \text{eV})$ is significantly lower than the MCDF result $\nu_{^3P_0^o} = 9.3127\ (-2.3957\ \text{eV})$ [32]. States with higher orbital angular momentum, such as $^3P_2^e\ 5g_{7/2}$, $^1D_2^e\ 5g_{7/2}$, are all readily calculated by our method, which were not included in previous MCDF treatments [32].

C. Properties of the autoionization states

In the autoionization region, some channels are closed with others opened. From the smooth MQDT parameters shown in Fig. 2, we can readily get resonant scattering matrices for

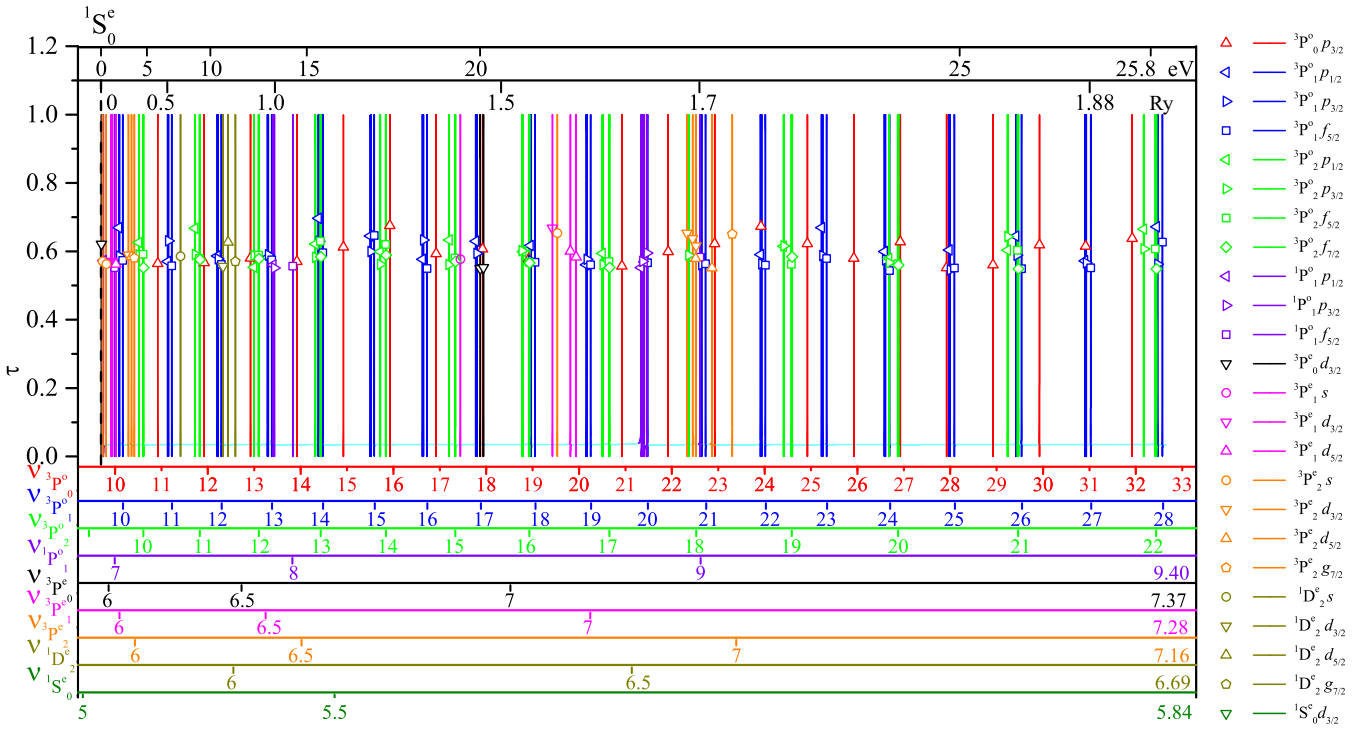

FIG. 4. Eigenphase shifts (effective eigenchannel quantum defects) in the autoionization energy range $\nu_{^3P^o_0} = 9.7 \sim 33$ ($0 \sim 26$ eV). Colored symbols indicate autoionization resonance positions at maxima of the energy derivatives of eigenphase shifts.

autoionization with the channel projection method [20,21], from which we can obtain all related autoionization quantities [33–41]. Notably, eigenphase shifts, which are eigenvalues of resonant scattering matrices, are crucial for the determination of resonance properties [34,40,41]. In the following, we will use eigenphase shifts to demonstrate complex autoionization structures of highly charged Ar^{13+} ions using our R-R-eigen method. Specifically, using the analytical properties of Coulomb wave functions [20], we can readily calculate eigenphase shifts of resonant scattering matrices from MQDT parameters without the need to diagonalize the physical scattering matrices [13,16–21]. Let us denote the number of channels which satisfy the closed channel boundary condition as N_c and open channels as N_o; thus the asymptotic boundary conditions require

$$\sum_\alpha U_{i\alpha} \sin \pi(\nu_i + \mu_\alpha) A^\rho_\alpha = 0, \quad i \in N_c \text{ closed channels}, \tag{8a}$$

$$\sum_\alpha U_{i\alpha} \sin \pi(-\tau_\rho + \mu_\alpha) A^\rho_\alpha = 0, \quad i \in N_o \text{ opened channels}, \tag{8b}$$

with N_c effective principal quantum numbers ν_i [see Eq. (5)] and τ_ρ the ρth eigenchannel quantum defect for N_o opened channels (i.e., collisional phase shift)]. The MQDT equation [Eq. (6)] is now generalized as

$$F(\{x_i\}, \{U_{i\alpha}, \mu_\alpha\}) = \det[U_{i\alpha} \sin \pi(x_i + \mu_\alpha)] = \det(F_{i\alpha}) = 0, \tag{9}$$

where $x_i = \nu_i$ for $i \in N_c$ closed channels, and $x_i = -\tau_\rho$ for $i \in N_o$ opened channels. The solutions of Eqs. (5) and (9) will lead to N_o resonant eigenphase shifts $\pi\tau_\rho$, from which various properties (resonance positions, widths, etc.) of the autoionization states can be obtained [40,41].

Applying the MQDT procedure [i.e., Eqs. (5) and (9)], the effective eigenchannel quantum defect (resonant eigenphase shifts $\pi\tau_\rho$) in the autoionization energy region $\nu_{^3P^o_0} = 9.7 \sim 33$ ($0 \sim 26$ eV) is obtained (see Fig. 4). The same as in Fig. 3, different colors and symbols of solution curves represent ionization channel characteristics including targets and channel electrons. Auxiliary abscissas $\nu_{^3P^o_0}$, $\nu_{^3P^o_1}$, $\nu_{^3P^o_2}$, $\nu_{^1P^o_1}$, $\nu_{^3P^e_0}$, $\nu_{^3P^e_1}$, $\nu_{^3P^e_2}$, $\nu_{^1D^e_2}$, and $\nu_{^1S^e_0}$ are also plotted to identify resonance states conveniently. The black dashed line at $\nu_{^3P^o_0} = 9.6982$ indicates the position of the first threshold $^1S^e_0$. There is only one opened channel $^1S^e_0\, d_{3/2}$ ("horizontal" cyan curve) observed; the other closed channels associated with higher thresholds $^3P^o_{0,1,2}$, $^1P^o_1$, $^3P^e_{0,1,2}$, $^1D^e_2$, $^1S^e_0$ (red, blue, green, violet, black, magenta, orange, dark yellow, and olive curves) are plotted as steep rises of the phase shift τ_ρ at $\nu \approx$ integer. It can be seen that the lowest principal quantum numbers for autoionization resonance series $^3P^o_{0,1,2}\, nl$, $^1P^o_1\, n'l'$ and $^3P^e_{0,1,2}$, $^1D^e_2$, $^1S^e_0\, n''l''$ are 10, 7, and 6, respectively. These autoionization resonances make up the intermediate states of the electron-ion recombination process. Especially, the intrashell two-electron excited ($2s^2 \to 2p^2$) resonance series $2p^2\ ^3P^e_{0,1,2}$, $^1D^e_2$, $^1S^e_0\, n''l''(n'' \geqslant 6)$ are attributed to the strong trielectronic recombination (TR) rate coefficients [7]. Based on the analytical property, we can easily obtain all relevant autoionization resonances ($n \to \infty$) to show the quasiperiodicity by its effective quantum number ν. For example,

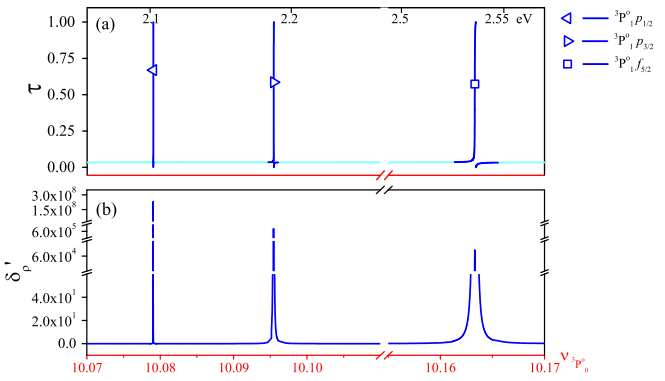

FIG. 5. Eigenphase shifts and corresponding energy derivatives in the energy region $\nu_{^3P_0^o} = 10.07 \sim 10.17$: (a) zoom-in details of autoionization resonances and (b) energy derivatives of corresponding eigenphase shifts.

several red steep resonances $^3P_0^o\, np_{3/2}$ show up periodically at $\nu_{^3P_0^o}$=integer ($10 \sim 33$). Since autoionization resonances are based on scattering matrices with accuracies checked using precision spectroscopic levels, hopefully they can be used as benchmark data to supplement the future experimental data.

Let us return to discuss the determination of autoionization resonance positions and widths, which are important physical parameters in many applications. As shown in Fig. 4, with the aid of the calculated ionization channel mixing coefficients of the eigenenergy wave functions, we can trace the characteristics of each individual resonance. These features are very helpful for treating the overlapping resonances (common in strong correlated systems), which allow us to disentangle the "isolated" resonance from the possible overlapping resonances. Then resonance positions and widths are obtained without the need for any fitting procedures based on the isolated resonance approximation [33,36,40,41]. More specifically, the theoretical resonance positions $(\nu^{\rm res}_{^3P_0^o}, \tau^{\rm res}_\rho)$ can be defined as the position of the maxima of the energy derivatives of the eigenphase shift $\delta'_\rho = d\delta_\rho/dE = \pi d\tau_\rho/d(I_{^3P_0^o} - 14^2/\nu^2_{^3P_0^o})$, which are plotted as colored open circles. Corresponding resonance widths are the inverse of the maxima δ'_ρ, namely, $\Gamma = 2/\delta'_{\rm max}(E_{\rm res})$ [34,40,41]. For a more intuitive understanding, Figs. 5(a) and 5(b) display zoom-in details of autoionization resonance phase shifts τ_ρ and corresponding energy derivatives δ'_ρ for three resonances series in the autoionization energy region $\nu_{^3P_0^o} = 10.07 \sim 10.17$. As indicated in Fig. 5(b), the linewidth

TABLE II. Comparisons of resonance positions by ν and $E_{\rm res}$ (in eV), autoionization widths Γ (in meV) of autoionization states ($0 \sim 10$ eV) between R-R-eigen and FAC results. The corresponding quantum defect values μ_R and $\mu_{\rm FAC}$ (5th and 8th columns) are also listed for convenient comparison, where "Diff" denotes the difference $\mu_{\rm FAC} - \mu_R$. Normalized ionization channel mixing coefficients A_i^2 are listed for three states $|a\rangle$, $|b\rangle$, and $|c\rangle$ with strong channel interactions.

	R-R-Eigen				FAC				A_i^2			
States	ν	$E_{\rm res}$	Γ	μ_R	$E_{\rm res}$	Γ	$\mu_{\rm FAC}$	Diff	A_1^2	$Channel_1$	A_2^2	$Channel_2$
$^3P_0^e\, 6d_{3/2}$	9.708	0.060	2.51×10^{-3}	0.035	0.566	2.6×10^{-2}	0.079	0.044				
$\|a\rangle$	9.729	0.179	1.07×10^{-2}	0.142	0.810	6.72×10^{-4}	0.175	0.033	0.50	$^3P_2^e\, 6s_{1/2}$	0.40	$^1P_1^o\, 7p_{3/2}$
$^1P_1^o\, 7p_{1/2}$	9.748	0.288	1.85×10^{0}	0.085	1.543	1.80×10^{0}	0.099	0.014				
$\|b\rangle$	9.810	0.642	5.33×10^{-2}	0.063	1.643	2.87×10^{-1}	0.093	0.030	0.30	$^1P_1^o\, 7_p 3/2$	0.66	$^3P_2^e\, 6s_{1/2}$
$\|c\rangle$	9.915	1.226	4.24×10^{-2}	0.085	1.013	5.65×10^{-3}	0.203	0.118	0.44	$^3P_0^o\, 10p_{3/2}$	0.46	$^3P_1^e\, 6d_{3/2}$
$^3P_1^e\, 6d_{3/2}$	9.936	1.341	1.55×10^{-2}	0.034	1.780	4.66×10^{-3}	0.076	0.042				
$^1P_1^o\, 7f_{5/2}$	9.990	1.633	1.04×10^{-1}	0.000	2.997	2.84×10^{-1}	0.008	0.007				
$^3P_1^e\, 6d_{5/2}$	10.018	1.780	9.67×10^{-2}	0.017	2.239	1.16×10^{-2}	0.058	0.041				
$^3P_1^o\, 10p_{1/2}$	10.079	2.102	3.96×10^{-5}	0.088	2.001	1.06×10^{-1}	0.184	0.096				
$^3P_1^o\, 10p_{3/2}$	10.095	2.188	1.38×10^{-2}	0.072	1.892	1.47×10^{-1}	0.203	0.131				
$^3P_0^o\, 10f_{5/2}$	10.163	2.536	1.15×10^{-1}	0.007	2.286	1.97×10^{-1}	0.133	0.126				
$^3P_2^e\, 6d_{3/2}$	10.287	3.153	8.05×10^{-4}	0.027	3.584	3.93×10^{-3}	0.069	0.042				
$^3P_2^e\, 6d_{5/2}$	10.354	3.480	2.51×10^{-1}	0.014	3.883	1.54×10^{-1}	0.058	0.044				
$^3P_2^e\, 6g_{7/2}$	10.416	3.771	1.79×10^{-3}	0.002	4.170	1.78×10^{-3}	0.046	0.044				
$^3P_2^o\, 10p_{1/2}$	10.510	4.213	1.65×10^{-4}	0.083	3.959	2.76×10^{-3}	0.199	0.116				
$^3P_2^o\, 10p_{3/2}$	10.516	4.237	1.97×10^{-4}	0.079	4.105	3.06×10^{-2}	0.174	0.095				
$^3P_2^o\, 10f_{5/2}$	10.604	4.637	1.35×10^{-2}	0.004	4.355	1.82×10^{-3}	0.129	0.124				
$^3P_2^o\, 10f_{7/2}$	10.615	4.687	5.73×10^{-1}	−0.005	4.453	1.07×10^{0}	0.111	0.116				
$^3P_0^o\, 11p_{3/2}$	10.922	5.997	4.26×10^{-3}	0.078	5.752	1.10×10^{-2}	0.243	0.165				
$^3P_1^o\, 11p_{1/2}$	11.134	6.840	1.03×10^{-5}	0.090	6.581	1.07×10^{-4}	0.255	0.165				
$^3P_1^o\, 11p_{3/2}$	11.151	6.905	3.80×10^{-3}	0.074	6.668	1.16×10^{-2}	0.234	0.160				
$^3P_1^o\, 11f_{5/2}$	11.221	7.175	9.28×10^{-2}	0.007	6.909	1.04×10^{-1}	0.177	0.170				
$^1D_2^e\, 6s_{1/2}$	11.412	7.877	2.51×10^{-6}	0.139	9.267	2.19×10^{-3}	0.168	0.029				
$^3P_2^o\, 11p_{1/2}$	11.723	8.948	5.23×10^{-4}	0.084	8.656	4.28×10^{-3}	0.248	0.163				
$^3P_2^o\, 11p_{3/2}$	11.727	8.961	1.04×10^{-3}	0.081	8.670	6.54×10^{-4}	0.244	0.163				
$^3P_2^o\, 11f_{5/2}$	11.821	9.270	1.46×10^{-2}	0.005	8.978	1.53×10^{-2}	0.172	0.167				
$^3P_2^o\, 11f_{7/2}$	11.831	9.301	3.54×10^{-1}	−0.003	9.016	4.98×10^{-1}	0.163	0.166				
$^3P_0^o\, 12p_{3/2}$	11.922	9.591	4.78×10^{-3}	0.078	9.393	1.27×10^{-2}	0.278	0.200				

of the first resonance is about 3 orders of magnitude smaller than other two narrow resonances, which clearly demonstrates the merit of our R-R-eigen method, i.e., all autoionization resonances can be calculated without missing any one for the complex HCI system.

In Table II, we list calculated resonance positions by ν and $E_{\rm res}$ (in eV), autoionization widths Γ (in meV) of autoionization states within the resonance energy $0 \sim 10$ eV. It should be mentioned that some autoionization states near the threshold strongly depend on electron-electron interactions between bound states and continuum states, where strong channel interactions exist and are not possible to designate using a single channel character. For these special resonant states, i.e., $|a\rangle$, $|b\rangle$, and $|c\rangle$ (see last four columns in Table II), we also give normalized mixing coefficients A_i^2 of ionization channels for clarity. As a comparison, simple flexible atomic code (FAC) results are also presented based on relativistic configuration interactions (RCI) method under the DW approximation [42], where configurations $(2s^2, 2s2p, 2p^2)nl, n = 2 \sim 12$ of B-like Ar^{13+} ions are considered. Large discrepancies can be easily found in both resonance positions and linewidths between these two methods. In addition to the difference in values of these quantities, we can also notice the change of configuration mixings between these two results. More specifically, the energy order of some resonance states calculated by FAC is different from those by R-R-eigen, especially for those associated with higher $^1P^o$, $^3P^e$, and $^1D^e$ thresholds. We found that for about 1/3 states listed in Table II, the linewidths calculated by the FAC are smaller than those by R-R-eigen, while others are larger. It is interesting to note that these 1/3 states are also associated with higher $^1P^o$, $^3P^e$ thresholds. For the present strongly correlated systems, these discrepancies exactly reflect the difficulty in electron correlation calculations, as well as the difference between these two methods in dealing with electron correlation effects.

Since there are no available experimental values, it is hard to determine which result is "correct." Next, we will try to assess the validity of these two results from the physical features of excited states in atomic systems. Based on the MQDT [15–21], which can serve as a unified theoretical framework to describe resonance states across ionization thresholds, the quantum defect $\mu = n - \nu$ [with the ν defined in Eq. (5)] is a key physical quantity for excited states. The quantum defect measures the short-range phase shift (compared with the wave under the pure Coulomb potential) of an excited electron due to many-body interactions within the reaction zone. Because of the dominant centrifugal potential around the atomic nucleus, for excited electrons within a same channel (i.e., can be identified with the same ion-core state and angular momentum), when the excitation energy varies in a range of our interest, the relative variation of their local momentums in the short range is very small. As a result, energy-normalized wave functions of channel electrons within the reaction zone are nearly the same. Therefore, excited electrons in a channel share some similarities in physical quantities such as quantum defects μ, oscillator strength densities, etc., which we refer to as "channel properties" in later discussions.

For the R-R-eigen method, the effective quantum defects can be readily calculated from the ν, whereas for the RCI method used in the FAC, additional calculations of ion-core energies with appropriate configurations are required to extract corresponding quantum defects. Our previous experience [43] is taken into account in configuration selection processes of these RCI calculations, where $2l2l'$ and $2l3l'$ of Be-like Ar^{14+} ions are adopted. Calculated quantum defect values are shown in Table II (μ_R and $\mu_{\rm FAC}$ in the 5th and 8th columns, respectively). It can be seen that $\mu_{\rm FAC}$ values are generally 0.16 and 0.04 larger than μ_R for $2s2pnl$ series (DR channels) and $2p^2nl$ series (TR channels [7]), respectively. Considering the electron correlation model used in the FAC calculation is relatively simple (with only limited configurations and without the use of pseudo-orbitals), the large quantum defects in FAC results indicates they are still away from the final convergence. Furthermore, we can deduce that R-R-eigen results should be more reasonable based on the following three facts: (1) All short-range scattering matrices for autoionization calculations are checked to be in good agreement with available experimental results in bound energy regions. (2) There exist good channel properties for μ_R within the same Rydberg series (i.e., slowly changing with increasing energy), which is not true for $\mu_{\rm FAC}$. (3) For resonances related to high l electrons (such as d or f waves), the large centrifugal potential makes the electron wave difficult to penetrate into the inner region and results in a small quantum defect. R-R-eigen results satisfy this physics picture qualitatively, whereas FAC results do not. Taking the f wave as an example, μ_R values are in the order of 10^{-3} while $\mu_{\rm FAC}$ are in the order of 10^{-1}, which are even comparable with quantum defects of s waves. Due to the limitation of experimental resolution, there maybe be dozens of autoionization states contributing to an isolated resonance peak of recombination spectra. The individual resonance may have a substantial influence on the observed spectra, which may lead to obvious differences between configuration interaction (CI) results under the DW approximation and our calculations. Therefore, the R-R-eigen method provides us great promise to improve theoretical calculations for the recent electron-ion recombination experiment of Be-like Ar^{14+} ions at CSRm and to explain substantial discrepancies between measured spectra and AUTOSTRUCTURE results [7].

III. CONCLUSIONS

Strong electron correlations within $2s$, $2p$ shells in highly charged B-like Ar^{13+} ions are demonstrated with the example of $J^\pi = 1.5^+$ symmetry, which are very different from the neutral B atom and beyond the qualitative impression of less prominent electron correlations in highly charged ions (HCIs). Strong intrashell correlations in Ar^{13+} ions manifest as an atomic system with many channel interactions. Specifically, there are 25 strong interacted channels in bound and adjacent autoionization energy regions which show obvious differences with the B atom with only one channel. In the language of the CI method, this kind of strong correlated behaviors means strong interaction among different reference configurations. Due to the variational nature of the CI method, the quality of excited-state calculations closely depends on the quality of lower states. In highly correlated systems, subtle changes in lower states due to the insufficient treatment of electron correlations will result in a large difference in excited states. On

the other hand, treatments of the excited atomic system in the eigenchannel *R*-matrix method start from its corresponding ion core with finite excitations. Interactions between bound or adjacent continuum excited electrons with the ion core are calculated in a unified way by a quasicomplete basis within the reaction zone.

We show in this paper that the relativistic eigenchannel *R*-matrix method can be successfully applied to B-like Ar^{13+} ions. Accurate short-range scattering matrices (i.e., MQDT parameters of eigenquantum defects μ_α and Euler-type angles θ_k) in both discrete and continuum regions are calculated. Applying MQDT procedures, all energy levels of the bound states are obtained without missing any one. Using the pro*j*ected ***h***igh dimensional qu***an***tum-defect ***g***raph (symmetri*z*ed) (i.e., the JHANGZ plot) for atomic systems with many thresholds (more than two), we can check and/or calibrate scattering matrices in a discrete energy region. A good agreement is found between calculated energy levels and available spectroscopy data [29,31], which indicates that our results are better than previous MCDF results [32]. The good quality of short-range scattering matrices also allows us to predict properties of adjacent autoionization resonances. As a demonstration example, theoretical resonance positions and autoionization widths of autoionization states in $0 \sim 26$ eV are calculated using maxima of energy derivatives of eigenphase shifts [40,41]. The comparison for autoionization states between our results and FAC calculations shows a large discrepancy, which gives an alternative evidence that strong electron correlations play a crucial role in theoretical calculations of highly charged Ar^{13+} ions.

It should be interesting to extend the studies in this work for the electron-ion recombination process of Be-like Ar^{14+} ions at the CSRm, where a substantial difference existed between the DW calculations using the AUTOSTRUCTURE code and the experimental results, especially at low resonance energies [7]. Based on the framework of the well-established perturbative treatment of the DR process, the DR rates depend on two physical parameters, namely, electron-capture rates and radiative decay rates [42,44]. The rates for the electron-capture process (i.e., the inverse of the autoionization process) can be readily calculated by the procedure adopted in this work. The radiative decay rates can be calculated similarly to the method demonstrated in one of our earlier works [11] using the R-eigen method. Note that for the calculation of recombination processes, all contributions from the doubly excited intermediate states with different J^π as well as a large number of final states of the radiative decay processes below the first threshold $2s^2\ {}^1S_0^e$ need to be considered, which are still in progress. It is believed that the R-R-eigen calculations can give a better analysis of the measured spectra and shape a more detailed understanding of the recombination resonances.

ACKNOWLEDGMENTS

This work is partly supported by the National Key R&D Program of China under Grants No. 2017YFA0402300 and No. 2016YFA0302104, the National Natural Science Foundation of China under Grants No. 11774023 and No. U1930402, the Strategic Priority Research Program of the Chinese Academy of Sciences through Grants No. XDB21030300 and No. XDPB09-02, the Key Research Program of Frontier Sciences, CAS, through Grant No. QYZDY-SSW-SLH006, and the National High-Tech ICF Committee in China. We also acknowledge computational support provided by the Beijing Computational Science Research Center. R.J. would like to thank the Helmholtz-OCPC International Postdoctoral Exchange Fellowship Program for support.

[1] P. Beiersdorfer, J. Phys. B: At. Mol. Opt. Phys. **48**, 144017 (2015).
[2] T. R. Kallman and P. Palmeri, Rev. Mod. Phys. **79**, 79 (2007).
[3] J. Dubau and S. Volonte, Rep. Prog. Phys. **43**, 199 (1980).
[4] K. Lagattuta and D. Winske, J. Quant. Spectrosc. Radiat. Transfer **58**, 703 (1997).
[5] M. F. Gu, S. M. Kahn, D. W. Savin, E. Behar, P. Beiersdorfer, G. V. Brown, D. A. Liedahl, and K. J. Reed, Astrophys. J. **563**, 462 (2001).
[6] K. P. Dere, E. Landi, P. R. Young, and G. D. Zanna, Astrophys. J. Suppl. Ser. **134**, 331 (2001).
[7] Z. K. Huang, W. Q. Wen, X. Xu, S. Mahmood, S. X. Wang, H. B. Wang, L. J. Dou, N. Khan, N. R. Badnell, S. P. Preval, S. Schippers, T. H. Xu, Y. Yang, K. Yao, W. Q. Xu, X. Y. Chuai, X. L. Zhu, D. M. Zhao, L. J. Mao, X. M. Ma *et al.*, Astrophys. J. Suppl. Ser. **235**, 2 (2018).
[8] X. Gao and J. M. Li, Chin. Phys. Lett. **29**, 033101 (2012).
[9] X. Gao and J. M. Li, Phys. Rev. A **89**, 022710 (2014).
[10] T. N. Chang, T. K. Fang, and X. Gao, Phys. Rev. A **91**, 023403 (2015).
[11] X. Gao, R. Jin, D. L. Zeng, X. Y. Han, J. Yan, and J. M. Li, Phys. Rev. A **92**, 052712 (2015).
[12] D. L. Zeng, R. Jin, C. Gu, X. F. Yue, X. Gao, and J. M. Li, Phys. Rev. A **95**, 042508 (2017).
[13] X. Gao, X. Y. Han, and J. M. Li, J. Phys. B: At. Mol. Opt. Phys. **49**, 214005 (2016).
[14] R. Jin, X. Y. Han, X. Gao, D. l. Zeng, X. Gao, and J. M. Li, Sci. Rep. **7**, 11589 (2017).
[15] U. Fano and C. M. Lee, Phys. Rev. Lett. **31**, 1573 (1973).
[16] C. M. Lee and K. T. Lu, Phys. Rev. A **8**, 1241 (1973).
[17] C. M. Lee, Phys. Rev. A **10**, 584 (1974).
[18] U. Fano, J. Opt. Soc. Am. **65**, 979 (1975).
[19] C. M. Lee and W. R. Johnson, Phys. Rev. A **22**, 979 (1980).
[20] M. J. Seaton, Rep. Prog. Phys. **46**, 167 (1983).
[21] M. Aymar, C. H. Greene, and E. Luc-Koenig, Rev. Mod. Phys. **68**, 1015 (1996).
[22] P. G. Burke, *R-Matrix Theory of Atomic Collisions: Application to Atomic, Molecular and Optical Processes* (Springer, Berlin, 2011).
[23] K. A. Berrington, W. B. Eissner, and P. H. Norrington, Comput. Phys. Commun. **92**, 290 (1995).
[24] K. Bartschat, Comput. Phys. Commun. **114**, 168 (1998).
[25] P. H. Norrington and I. P. Grant, J. Phys. B: At. Mol. Opt. Phys. **20**, 4869 (1987).

[26] S. Ait-Tahar, I. P. Grant, and P. H. Norrington, Phys. Rev. A **54**, 3984 (1996).
[27] O. Zatsarinny, Comput. Phys. Commun. **174**, 273 (2006).
[28] B. Edlén, Phys. Scr. **28**, 51 (1983).
[29] A. Kramida, Yu. Ralchenko, J. Reader, and NIST ASD Team, NIST Atomic Spectra Database (ver. 5.6.1), [Online]. Available: https://physics.nist.gov/asd [2019, March 11] (2018).
[30] See Supplemental Material at http://link.aps.org/supplemental/10.1103/PhysRevA.101.032508 for Fig. S1, the MQDT physical parameters (including eigenquantum defects μ_α and Euler angles θ_k) of the Ar^{13+} system with $J^\pi = 1.5^+$ in the energy regions ($-23.0 \leqslant E \leqslant 8.0$ Ry), and Table S1, the associated data for MQDT parameters.
[31] J. K. Lepson, P. Beiersdorfer, E. Behar, and S. M. Kahn, Astrophys. J. **590**, 604 (2003).
[32] K. M. Aggarwal, F. P. Keenan, and S. Nakazaki, A&A **436**, 1141 (2005).
[33] G. Breit and E. Wigner, Phys. Rev. **49**, 519 (1936).
[34] E. P. Wigner, Phys. Rev. **98**, 145 (1955).
[35] F. T. Smith, Phys. Rev. **118**, 349 (1960).
[36] K. Bartschat and P. G. Burke, Comput. Phys. Commun. **41**, 75 (1986).
[37] Y. L. Peng, X. Y. Han, M. S. Wang, and J. M. Li, J. Phys. B: At. Mol. Opt. Phys. **38**, 3825 (2005).
[38] D. T. Stibbe and J. Tennyson, Comput. Phys. Commun. **114**, 236 (1998).
[39] K. Aiba, A. Igarashi, and I. Shimamura, J. Phys. B: At. Mol. Opt. Phys. **40**, F9 (2007).
[40] L. Quigley and K. Berrington, J. Phys. B: At. Mol. Opt. Phys. **29**, 4529 (1996).
[41] L. Quigley, K. Berrington, and J. Pelan, Comput. Phys. Commun. **114**, 225 (1998).
[42] M. F. Gu, Can. J. Phys. **86**, 675 (2008).
[43] X. Wang, L. Liu, X. Gao, C. Shen, and J. Li, Chin. Phys. Lett. **25**, 4244 (2008).
[44] R. D. Cowan, *The Theory of Atomic Structure and Spectra* (University of California Press, Berkeley, 1981).